Ceramics International xxx (xxxx) xxx

Contents lists available at ScienceDirect

Ceramics International

journal homepage: www.elsevier.com/locate/ceramint

$Ca_{9.95}Li_{1.05}(PO_4)_7$ and β-$Ca_3(PO_4)_2$ lamellar microstructure: multilayer 3D scaffolds for 3T3 cell viability studies

M. Angélica Barbudo [a,*], Pablo Velásquez [a], Ángel Murciano [b], Piedad N. De Aza [a]

[a] Instituto de Bioingeniería, Universidad Miguel Hernández, Avda. Universidad S/n, Elche, Alicante, 03202, Spain
[b] Departamento de Materiales, Óptica y Tecnología Electrónica, Universidad Miguel Hernández, Avda. Universidad S/n, Elche, Alicante, 03202, Spain

ARTICLE INFO

Handling Editor: Dr P. Vincenzini

Keywords:
Scaffold
Biocompatibility
Surface modification
Tissue engineering

ABSTRACT

This study proposes the development of a lamellar microstructure in multilayer ceramic scaffolds to investigate the influence of surface morphology on cell behavior. The scaffolds consist of tricalcium silicate (C_3S) core and calcium phosphate outer coatings, where Ca ions are partially substituted with Li ions. The scaffolds were physicochemically characterized by X-ray diffraction (XRD), Field Emission Scanning Electron Microscopy with Energy Dispersive X-ray spectroscopy (FESEM/EDX) and Mercury Porosimetry. The scaffolds exhibited $Ca_2P_2O_7$, β-$Ca_3(PO_4)_2$, $Ca_{9.95}Li_{1.05}(PO_4)_7$, $CaLi(PO_4)$ and $Li_3(PO_4)$ as main phases. The $Ca_2P_2O_7$ phase in the outer layer was removed using a 30-s etching process, revealing a lamellar microstructure in the bulk. The compressive strength of the scaffolds was 1.2 ± 0.1 MPa for the control and 0.9 ± 0.1 MPa for the C30s scaffolds, while the corresponding microporosity values were 61 % and 72 %. In vitro bioactivity assays demonstrated hydroxyapatite-like (HA-like) precipitation on etched scaffolds after 14 days in simulated body fluid (SBF), unlike the untreated controls. Direct and indirect biological assays using 3T3 fibroblasts revealed significantly higher cell viability, adhesion, and proliferation on the scaffolds with the lamellar microstructure, futher enhanced by the HA-like coating. FESEM imaging confirmed cell colonization on the surface and within the internal lamellar framework, suggesting that this architecture supports cell infiltration and ECM formation. These findings highlight the functional relevance of the lamellar microstructure in promoting biointegration, positioning these scaffolds as promising candidates for bone tissue engineering.

1. Introduction

Tissue engineering currently faces significant challenges in developing materials that fulfill clinical and biological requirements. These materials must integrate physicochemical, biochemical, and cellular factors to enable the replacement of biological tissues [1–5]. A critical requirement is that such materials degrade appropriately and are replaced by newly formed tissues [5–7]. Achieving this goal necessitates the investigation of properties that directly influence cell–material interactions, including phase composition, surface characteristics, and porosity, among others [7–12].

Several studies have shown that modifying the surface properties of biomaterials, such as microstructure or surface roughness, significantly influences the modulation of cellular functions [8,12,13].

Modifying scaffold surfaces through chemical or physical treatments, such as etching or coating deposition, can improve cell adhesion, proliferation, and differentiation, enhance bioactivity by promoting the formation of an HA-like layer, and ultimately strengthen interactions with specific cell types such as fibroblasts or osteoblasts [8,13,14]. In this context, porous ceramic biomaterials have demonstrated considerable potential owing to their similarity to the mineral phase of bone and their ability to support cell growth.

Specifically, it is well established that the inorganic compound hydroxyapatite, found in the collagen matrix of human bone, promotes bone regeneration and growth. However, during the initial stages of this process, fibroblasts play an essential role in the formation of extracellular matrix (ECM) and other proteins, as well as in facilitating soft callus formation, the first step in bone healing [15–18]. These cells also produce connective tissue during healing and regulate tissue homeostasis, which is essential for maintaining the balance between ECM production and degradation, thereby preserving the integrity of the bone and surrounding tissue. In addition, they interact directly with osteoblasts and osteoclasts, the key cells responsible for bone formation and resorption, respectively [2,18].

* Corresponding author. Instituto de Bioingeniería, Universidad Miguel Hernández, Elche, Alicante, 03202, Spain.
E-mail addresses: mbarbudo@umh.es (M.A. Barbudo), pavelasquez@umh.es (P. Velásquez), amurciano@umh.es (Á. Murciano), piedad@umh.es (P.N. De Aza).

https://doi.org/10.1016/j.ceramint.2025.06.145
Received 10 April 2025; Received in revised form 23 May 2025; Accepted 10 June 2025
Available online 10 June 2025

To our knowledge, no study has evaluated the behavior of fibroblasts on a scaffold with dual-level surface morphology modulation, involving a microstructure first modified to reveal a lamellar microstructure and subsequently treated with HA-like deposition within the lamellar microstructure.

Therefore, in this study, we propose the development of scaffolds with a core composed of a Ca_3SiO_5 formulation that confers support and a macroporous structure. This core will be coated with calcium phosphate compositions ($Ca_4Li_4(PO_4)_4$), where calcium ions are partially replaced by lithium ions. Lithium ions can stimulate bone formation (osteogenesis), inhibit bone resorption, increase cell proliferation, and finally improve the mechanical properties [19–21].

Once obtained, the scaffolds will undergo chemical etching to modulate surface properties. Subsequently, they will be subjected to physicochemical characterization, followed by in vitro bioactivity assessment and evaluation of cell culture behavior using indirect (dissolution products) and direct (scaffold) assays.

2. Materials and methods

2.1. Materials preparation

Multilayer ceramic scaffolds were prepared using the sol-gel method combined with the polymeric sponge replication technique [22]. To obtain the multilayer scaffolds, the process was divided into two stages: Stage I, the core preparation; and Stage II, the outer layers preparation. Table 1 summarizes the reagents used in the preparation of the core and outer layers of the scaffold.

For the core, C_3S was used and formulated by mixing 10.5 mL of tetraethyl orthosilicate (TEOS- $Si(OC_2H_5)_4$, Aldrich), 5 mL of 97 % ethanol, 5 mL of distilled water, and 1 mL of 37 % hydrochloric acid (HCl, Ensure), the mixture was stirred for 10 min to initiate the hydrolysis reaction. At the same time, a second solution was prepared by combining 14.1 g of calcium carbonate ($CaCO_3$, Sigma), 15 mL of distilled water, and 15 mL of 37 % hydrochloric acid (HCl, Ensure), which was added to the initial mixture. The pH of the solution was adjusted to 2–3 by the gradual addition of HCl.

Polyurethane sponges cut into cylindrical shapes (20 ppi, 12.7 mm diameter, 10 mm high), were submerged in the sol-gel solution and oven-dried at 175 °C for 10 min. Once the first layer had dried, this process was repeated approximately 25 times to ensure the coating formation. Finally, the sponges were subjected to sintering in a furnace at 1050 °C with a heating rate of 18.5 °C/h. The temperature was maintained for 8 h and then cooled to room temperature within the oven.

After obtaining the initial scaffold, designated as the core, it was covered with outer layers. The $Ca_4Li_4(PO_4)_4$, formulation for the outer coating was prepared by mixing 12 mL of triethyl phosphate ($(C_2H_4)_3PO_4$ -TEP, Aldrich), 5 mL of ethanol 97°, 15 mL of distilled water, 15 mL of hydrochloric acid (HCl 37 %, Ensure), 7.05 g of calcium carbonate ($CaCO_3$, Sigma) and 2.60 g of lithium carbonate (Li_2CO_3, Scharlau). The pH of the solution was adjusted to 2–3 by the gradual addition of HCl.

Once the cores were coated, they were dried at 195 °C for 15 min. This process was repeated three times to avoid the elimination of core scaffold porosity. Subsequently, the scaffolds were subjected to sintering at a heating rate of 115 °C/h, reaching a final temperature of 1050 °C and maintaining it for 4 h before being cooled to room temperature within the furnace. This process was repeated two times.

Furthermore, a solution was prepared by dissolving acetic acid (CH_3COOH, PanReac) in distilled water with agitation to ensure complete chemical dissolution at a concentration of 3 %. The scaffolds were immersed in the etching solution with agitation to ensure uniform exposure. The scaffolds were chemically etched for 30 s to modify the microstructure. Then, the scaffolds were rinsed with distilled water to remove any residual chemicals and subjected to a 24-h drying process at 80 °C. Finally, the scaffolds chemically etched for 30 s were broken to observe the fresh fractured surface.

Table 1
Reagents are used in the preparation of the cores and outer coating.[a]

Formulation composition	$CaCO_3$ (g)	Li_2CO_3 (g)	Triethyl phosphate TEP (mL)	Tetraethyl orthosilicate TEOS (mL)
Ca_3SiO_5	14.1	–	–	10.5
$Ca_4Li_4(PO_4)_4$	7.1	2.6	12	–

[a] All the preparations were carried out with 20 mL of distilled water, 15 mL of HCl and 5 mL of ethanol to obtain 10 g of the formulation.

2.2. Scaffolds characterization

The mineralogical compositions of the powder material were evaluated by XRD using a Bruker-AXR D8 Advance with Cu-Kα radiation (1.541874 Å). Data were collected in the Bragg-Brentano theta-2theta (θ/2θ) geometry between 10° and 55° (2θ) in 0.05° steps with a counting time of 5 s per step. The data presented correspond to the 2θ range between 20° and 35°. The X-ray tube operated at 40 kV and 30 mA. The obtained diffractograms were analyzed using version 3.16 of the Match! 3 software. Semiquantitative analysis of the scaffold phases was performed using the relative intensity ratio method (RIR), and the diffractograms were compared to data from the Crystallography Open Database (COD).

The microstructure and morphology of the multilayer ceramic scaffolds were studied by FESEM/EDX using a Zeiss SIGMA 300 VP equipped with Zeiss SmartEDX. All samples were coated with palladium prior to evaluation.

The porosity and pore size distribution (<300 μm) of the scaffolds were determined using mercury porosimetry (Poremaster 60 GT, Quantachrome Instruments) within a pressure range of 6.829 KPa to 243,658.266 KPa. Additionally, the porosity associated with pore sizes larger than 300 μm was measured using Archimedes' principle in mercury.

The maximum compressive strength of the scaffolds was measured using a simple manual test stand (SVL-1000N, IMADA). The load was manually applied to scaffolds (10 mm diameter, 9 mm high) until complete fracture occurred. The compressive strength of the ceramic scaffolds was calculated based on the results from five samples per batch.

2.3. In vitro bioactivity characterization

In vitro bioactivity assays of the scaffolds were performed by immersing them in SBF according to the procedure established by Kokubo et al. [23] and following ISO 23317:2014. Samples in SBF were incubated in a water bath at 37 °C for 1, 3, 7, and 14 days.

After each period, scaffolds were dried at 80 °C for 24 h and using FESEM/EDX. The SBF aliquots were assessed by inductively coupled plasma optical emission spectrometry (ICP-OES Thermo iCAP 6500 DUO) to study variations in calcium (Ca^{2+}), lithium (Li^{+}), silicon (Si^{4+}), and phosphorus (P^{5+}) ion concentrations.

2.4. In vitro biological evaluation

The behavior of the scaffolds—(i) Control (C), (ii) C30s, and (iii) C30s/14d—toward the cells in vitro was evaluated according to ISO 10993. In this study, cell viability was examined directly by exposing 3T3 cells (mouse embryonic fibroblasts) to the scaffold, and indirectly by assessing the indirect impact of scaffold dissolution products (DP) in DMEM on the cells.

3T3 cells were cultured in Petri dishes with Dulbecco's modified Eagle's medium (DMEM, Gibco) supplemented with 10 % fetal bovine

serum (FBS, Corning) and 1 % penicillin/streptomycin (PS, Gibco), incubated at 37 °C in a humidified atmosphere with 5 % CO_2.

Control scaffolds, as well as C30s and C30s/14d, were sterilized at 150 °C for 3 h and exposed to UV light on each side for 4 h.

2.4.1. Indirect cell culture

2.4.1.1. Ion release. To study the influence of ions released by the scaffolds—(i) Control, (ii) C30s, and (iii) C30s/14d—on the cells, the scaffolds were incubated in DMEM supplemented with 10 % FBS and 1 % PS. Dissolution products were prepared by adjusting the weight of each sample to a concentration of 50 mg/mL. Samples were incubated for 48 h (DP2) and 96 h (DP4), and an aliquot from each was analyzed by ICP-OES to determine the types of ions released by each material.

2.4.1.2. Cell culture and viability. 3T3 cells were seeded in 96-well plates at a concentration of 25,000 cells/ml one day prior to the indirect assay to ensure cell adherence.

Subsequently, the original culture medium was replaced with a conditioned culture medium containing the dissolution products DP2 and DP4. Finally, the cells were incubated at 37 °C in a humidified atmosphere with 5 % CO_2 for 24, 48 and 72 h. The Alamar blue assay was then performed, and absorbance was measured at 570 nm using an OPTIC IVYMEN SYSTEM Microplate Reader 2100-c. The control for this assay consisted of cells cultured in contact with DMEM medium supplemented with 10 % FBS and 1 % PS.

2.4.2. Direct cell culture

2.4.2.1. Sample preparation and cell seeding. After sterilization, samples were pre-conditioned and placed inside a 24-well plate with 1.5 mL of DMEM supplemented with 10 % FBS and 1 % PS and incubated for 45 min at 37 °C and 5 % CO_2. After the pre-conditioning period, the DMEM supplemented with 10 % FBS and 1 % PS was removed, and 50,000 cells in 25 μL were seeded dropwise onto the surface of each scaffold. The scaffolds were incubated for 30 min at 37 °C and 5 % CO_2. After these 30 min, fresh DMEM supplemented with 10 % FBS and 1 % PS was added to each well. Samples were incubated for 24, 48, and 72 h. The medium was refreshed daily.

2.4.2.2. Cell viability. The Alamar Blue assay was used to assess cell viability on each scaffold. The supplemented DMEM was removed, and the scaffolds were transferred to a new 24-well plate to avoid including cells attached to the bottom of the original wells. A solution containing 10 % of the culture volume of Alamar Blue® was then added to each well and incubated for 3 h at 37 °C in a 5 % CO_2 atmosphere. Then, 100 μL from each well was transferred to a 96-well plate, and absorbance was measured at 570 nm. The control for this assay consisted of cells seeded directly onto the plate.

2.4.2.3. Cell morphology evaluation. The evaluation of cell morphology and adhesion on the scaffold surface was performed using FESEM. The cells on the samples that exhibited the highest absorbance at 72 h were fixed with a 4 % paraformaldehyde solution for 30 min. Next, the scaffolds were washed three times with PBS (phosphate-buffered saline) to remove any residual formaldehyde.

Subsequently, the PBS was removed, and the samples were incubated in a 4 % osmium tetraoxide (OsO_4) solution for 1 h at room temperature in the dark to avoid photodegradation. The solution was then removed, and the scaffolds were washed three times with distilled water to eliminate any residual OsO_4. Next, a dehydration process was carried out using a graded ethanol series from 30 % to 100 % for 15 min. Finally, the scaffolds were submerged in acetone, dried using critical point drying (Balzers CPD 030) and observed using FESEM (SIGMA 300 VP, Zeiss). These scaffolds were also fractured and examined by FESEM.

2.4.2.4. Statistics. The results are presented as mean values with standard deviations. Statistical significance between groups was determined using two-way analysis of variance (ANOVA) followed by a Tukey test. The significance level was set at $p < 0.05 = *$.

3. Results

3.1. Scaffolds characterization

The mineralogical characterization performed using XRD to examine the crystalline phases present in the scaffolds is shown in Fig. 1 (a) control and Fig. 1 (b) C30s. Both are composed of the same main phases: $Ca_2P_2O_7$ (COD: 96-100-1557), β- $Ca_3(PO_4)_2$ (COD: 96-151-7239), $Ca_{9,95}Li_{1,05}(PO_4)_7$ COD: 96-152-6054), $CaLi(PO_4)$ (COD: 96-152-6054) and Li_3PO_4 (COD: 96-901-1045). In addition, both samples exhibited minority silicon phases such as SiO_2 (COD: 96-900-9688), Li_4SiO_4 (COD: 96-153-2524), Ca_2SiO_4 (COD: 96-210-3317) and $CaSiO_3$ (COD: 96-900-5779). Table 2 shows the percentage of each phase present.

The diffractograms presented in Fig. 1 (b) show a decrease in the peaks corresponding to the $C_2P_2O_7$ phase in the C30s scaffolds compared to the control, Fig. 1 (a), around the 2θ angles of 27°, 27.5° and 31°. As shown in Table 2, the proportion of the $Ca_2P_7O_2$ phase decreases markedly from 29 % to 12 %, indicating that chemical etching can effectively modulate the ratio of these phases.

Fig. 2 (a-c) illustrates the microstructure of the control, formed by large grains in which a lamellar structure can be inferred from the scratches on the surface of the scaffold, which appear to be covered by a glassy layer. Fig. 2 (d-f) corresponds to the surface of the C30s scaffold, where a lamellar microstructure is revealed across the entire surface. The same figure (g–i) depicts the inner part of the scaffold, revealing the same lamellar microstructure in bulk. EDX analysis of the control surface confirmed the presence of calcium and phosphorus, with a Ca/P ratio ranging from 1.04 ± 0.07 to 1.4–1.5.

The EDX analysis of C30s showed the presence of calcium and phosphorus, with an almost constant Ca/P ratio of 1.4 ± 0.02. In the case of the fresh fracture, the surface EDX analysis revealed a Ca/P ratio between 1.4 and 1.5. The most calcium-deficient areas corresponded to protruding lamellar structures on the surface, while the surrounding material was richer in calcium.

The combination of the revealed lamellar microstructure—which mimics the architecture of natural bone—and the previously described mineralogical composition are key factors in enhancing cell adhesion and proliferation on the scaffolds.

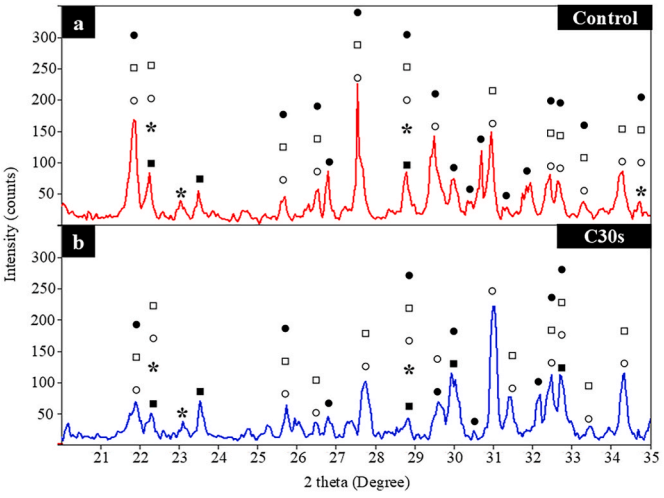

Fig. 1. XRD patterns of the multilayer scaffolds (a) Control and (b) C30s. (Main phases: • $Ca_2P_2O_7$, ○ β-$Ca_3(PO_4)_2$, □ $Ca_{9,95}Li_{1,05}(PO_4)_7$, ■ $CaLi(PO_4)$ and * $Li_3(PO_4)$.

Table 2
RIR analysis of the phases in the scaffolds.

Sample	$Ca_2P_2O_7$	β-$Ca_3(PO_4)_2$	$Ca_{9,95}Li_{1,05}(PO_4)_7$	$CaLi(PO_4)$	Li_3PO_4	Minority phases
	%					
Control	29	19	25	6	7	14
C30s	12	27	32	8	7	14

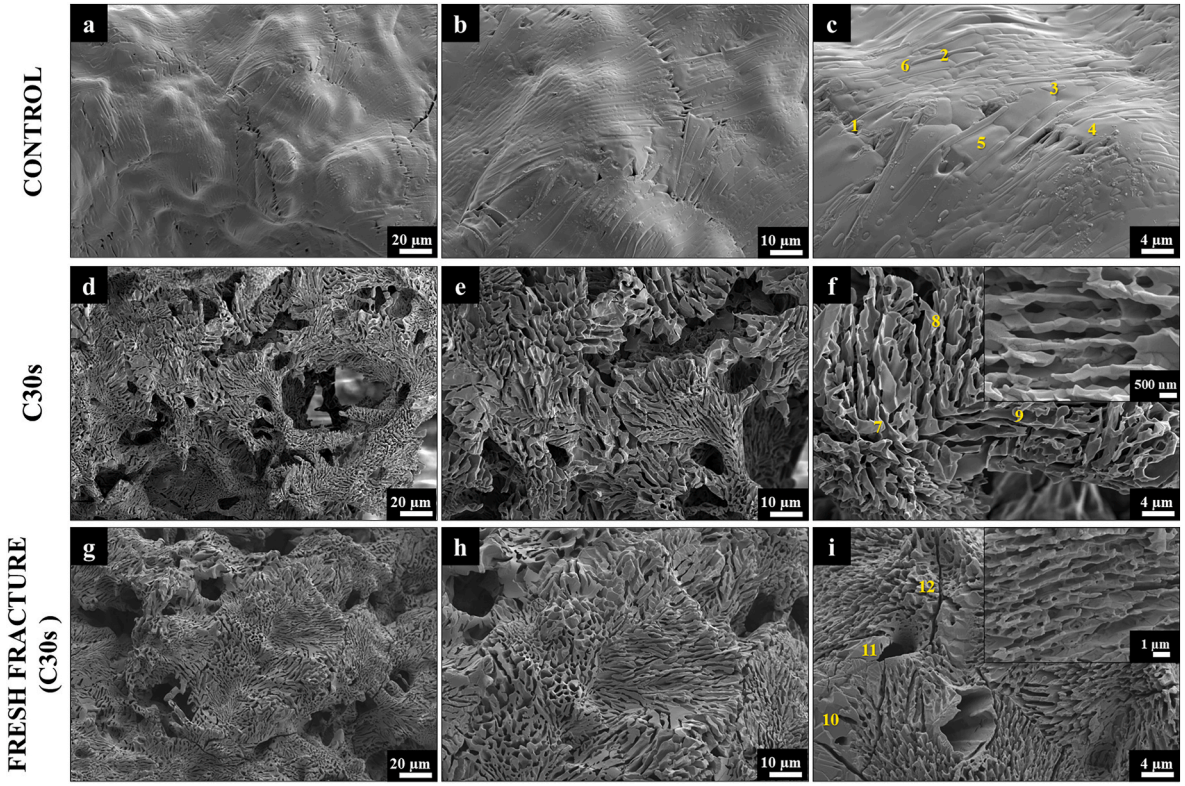

Fig. 2. FESEM micrographs of the scaffold surface: (a–c) control, (d–f) C30s and (g–i) C30s Fresh fracture.

Fig. 3 shows the results obtained from the porosity test and an optical image representative of the sintered scaffolds, which exhibit a pearlescent surface appearance. Table 3 presents a summary of the results obtained for porosity, compressive strength and lamellar width of the samples.

Fig. 3 (a) illustrates three regions describing the behavior of the control and C30s samples. For the control, the first region shows an increase in intruded mercury from 0 to 0.036 cc/g, corresponding to pore diameters ranging from 200 µm to 4.08 µm. This is followed by a plateau in intruded volume up to 1.09 µm, and then a second increase from 0.036 cc/g to 0.06 cc/g, corresponding to pore diameters between 1.09 µm and 0.02 µm. A similar pattern is observed for the C30s samples, with three distinct regions and a greater overall intruded volume.

Fig. 3 (b), shows that the control samples and C30s samples present different pore diameter peaks. For the control, these peaks occur around 99.23 µm, 6.31 µm, 0.20 µm, 0.07 µm and 0.04 µm. In contrast, the C30s samples exhibit the most significant intruded volume at pore diameters of approximately 170.60 µm, 8.50 µm, 4.76 µm and between 2.10 and 0.20 µm. In general, the C30s samples show a higher volume of intruded mercury at the aforementioned mentioned diameters.

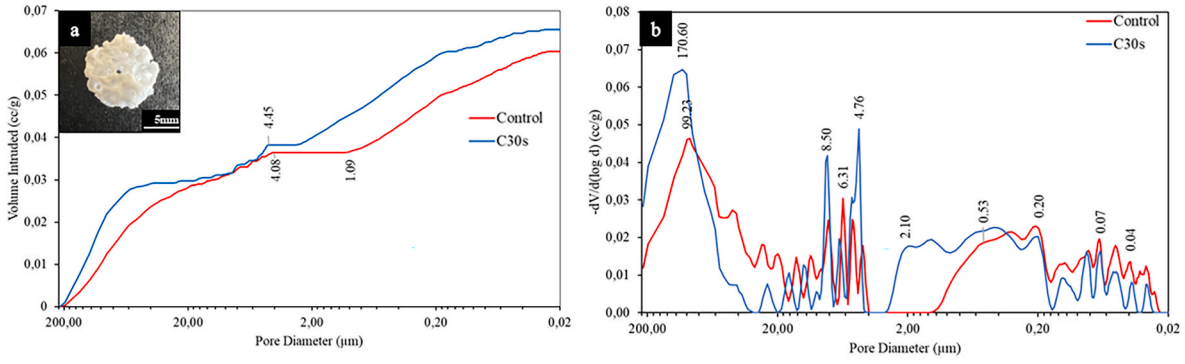

Fig. 3. Representative optical image of scaffolds (window). Mercury Porosimetry curves: (a) Cumulative and (b) Differential intrusion vs. pore diameter in scaffolds.

Table 3
Summary of the porosity, compressive strength and width of lamellar of the control and C30s scaffolds.

Sample	Porosity <300 μm[a]	Porosity >300 μm[b]	Compressive strength	Lamellar width
	(%)		MPa	nm
Control	14.5	61 ± 1	1.2 ± 0.1	–
C30s	15.5	72 ± 2	0.9 ± 0.1	200–500

[a] Obtained by the Mercury Porosimetry Technique.
[b] Obtained by Archimedes Principle in Mercury.

In addition, Table 3 shows that the micro-porosity (<300 μm) is within the same range for both samples; however, the macro-porosity (>300 μm) was higher for the C30s samples, 72 % ± 2, while for the controls, it was 61 % ± 1. This increase is a direct consequence of the removal of the vitreous phase, which unmasked larger pore openings and improved interconnectivity. While the compressive strength of the control samples—with lower macroporosity was—slightly higher (1.2 ± 0.1 MPa) than that of the C30s samples (0.9 ± 0.1 MPa), this reduction is expected owing to the increase in porosity and the elimination of the dense glassy phase, which previously contributed to structural rigidity. Finally, the C30s scaffolds presented a lamellar width between 200 and 500 nm. This nanoscale dimension can facilitate protein adsorption, focal adhesion formation and other essential factors for effective tissue regeneration.

3.2. In vitro bioactivity characterization

In relation to in vitro bioactivity, the scaffolds were tested by immersing them in SBF solution for 1, 3, 7, and 14 days. The control scaffolds did not show HA-like precipitates at any of the test times; however, the surface gradually degraded, revealing an incipient lamellar microstructure, as shown in Fig. 4. This suggests that the glassy surface layer in the control gradually dissolves in SBF, but not sufficiently to initiate apatite nucleation. In the case of the control submerged in SBF for 7 days, a small, dispersed precipitate was observed that contained phosphorus and calcium ions, with a Ca/P ratio of 1.36 ± 0.01, which disappeared after 14 days.

Fig. 4 also illustrates the surface of the C30s samples after immersion. These scaffolds did not exhibit significant changes in surface microstructure until 14 days, when a conglomerate of spherical deposits—similar to HA—precipitated, with a Ca/P ratio of 1.68 ± 0.01, consistent with stoichiometric hydroxyapatite (Ca/P ≈ 1.67). This confirms the bioactive nature of the chemically etched scaffolds, which are capable of inducing mineralization in a physiologically relevant environment.

To evaluate the concentrations of Ca, Li, Si, and P ions in the SBF, ICP-OES tests were performed. The results obtained for the samples at different test intervals are shown in Fig. 5. In both scaffolds, the concentration of Li ions gradually increased over 14 days, indicating that both scaffolds released Li ions.

In the case of the control, the following trends were observed: (i) From days 1–3, the concentrations of P and Si ions increased. (ii) On day 7, the concentration of P ions decreased, while the concentration of Si ions increased slightly. (iii) On day 14, the sample released P ions, increasing their concentration in the SBF, while absorbing Si ions and reducing their concentration to a level comparable to the initial SBF state. For the C30s samples, the results shown in Fig. 5. (b) indicate that, in general, the concentrations of P and Si ions increased up to day 7. However, on day 14, the sample absorbed P ions while releasing Si ions, forming a mirrored pattern opposite to that observed in the control.

3.3. In vitro biological characterization

Fig. 6 shows the release of ions in the culture medium for each material at a concentration of 50 mg/mL after 48 h and 96 h of incubation. In the dissolution products of the control and C30s scaffolds, a similar increase in lithium ion concentration was observed at both 48 h and 96 h. However, in the case of the C30s/14d scaffolds, the lithium ion concentration was nearly three times higher. Regarding the concentration of P ions, all scaffolds exhibited similar behavior, showing an increasing trend in the culture medium up to 96 h. However, in the dissolution products of the C30s/14d scaffolds, the P ion concentration decreased slightly at 96 h compared to 48 h, but it remained higher than in the initial culture medium.

Conversely, regarding Ca ions, all samples showed similar behavior. Up to 48 h, they slightly reduced the concentration of calcium ions in the medium. However, by 96 h, the Ca ion concentrations in both the control and C30s scaffolds remained similar to the initial levels in the culture medium.

Finally, the most significant differences were observed in the behavior of Si ions. In general, all scaffolds increased the concentration of Si ions, but the C30s/14d samples released these ions at a faster rate, while the control released Si ions more slowly and almost constantly.

The viability of the cells incubated with the different conditioned culture media is shown in Fig. 7. With the DP2 medium, after 24 h, cell viability increased significantly for the control scaffold and C30s/14d compared to the control cells, and this trend continued at 48 h and 72 h. Notably, the values obtained for the dissolution products of the control and C30s/14d scaffolds were markedly higher, as cell viability remained significantly higher compared to the control cells cultured in untreated medium. Significant differences were also observed between the C30s and the control cells after 48 h.

In the case of the dissolution products obtained at 96 h (DP4), significant differences were observed at 24 h between the control cells and the C30s/14d scaffolds. At 48 and 72 h, positive cellular behavior was observed for all scaffold dissolution products, similar to that of the control cells. These results confirm that the dissolution products are not only non-toxic but also bioactive, creating conditions that support and enhance fibroblast viability and activity.

After evaluating the influence of the ions released by the scaffolds on the cells, the behavior of the cells in direct contact with the control, C30s, and C30s/14d scaffolds was examined (Fig. 8). At 24 h, cell behavior in contact with the control and C30s scaffolds was similar to that of the control cells, whereas cells in contact with the C30s/14d scaffolds showed reduced proliferation. At 48 h, all scaffolds supported positive and increased cell proliferation, with no significant differences observed between them. After 72 h, the control cells and the cells seeded on the control scaffold exhibited similar absorbance values, indicating comparable levels of cell proliferation. In contrast, cells cultured on the C30s scaffolds—whose surface topography was modulated by chemical etching—showed increased absorbance, indicating enhanced proliferation due to the presence of lamellar structures. This effect was even more pronounced in cells exposed to the C30s/14d scaffolds, which showed a significantly higher absorbance signal. Furthermore, the results indicated that cell proliferation was higher in these scaffolds when compared to those assayed at 24 h. This enhanced cellular response can be attributed to several synergistic factors: (i) topographical cues provided by the 200–500 nm lamellae, which promote cell alignment and focal adhesion formation; (ii) the release of bioactive ions such as Li^{+} and Si^{4+}, which are known to stimulate osteogenic activity; and (iii) the presence of a biomimetic HA-like layer that replicates the mineral phase of natural bone extracellular matrix, promoting an osteoconductive environment.

As for morphological cell evaluation, tests were performed only on the C30s/14d scaffolds, which indicated higher cell proliferation at 72 h. Accordingly, FESEM images of the surface and fresh fracture are presented in Fig. 9. These images reveal that fibroblasts covered a large part

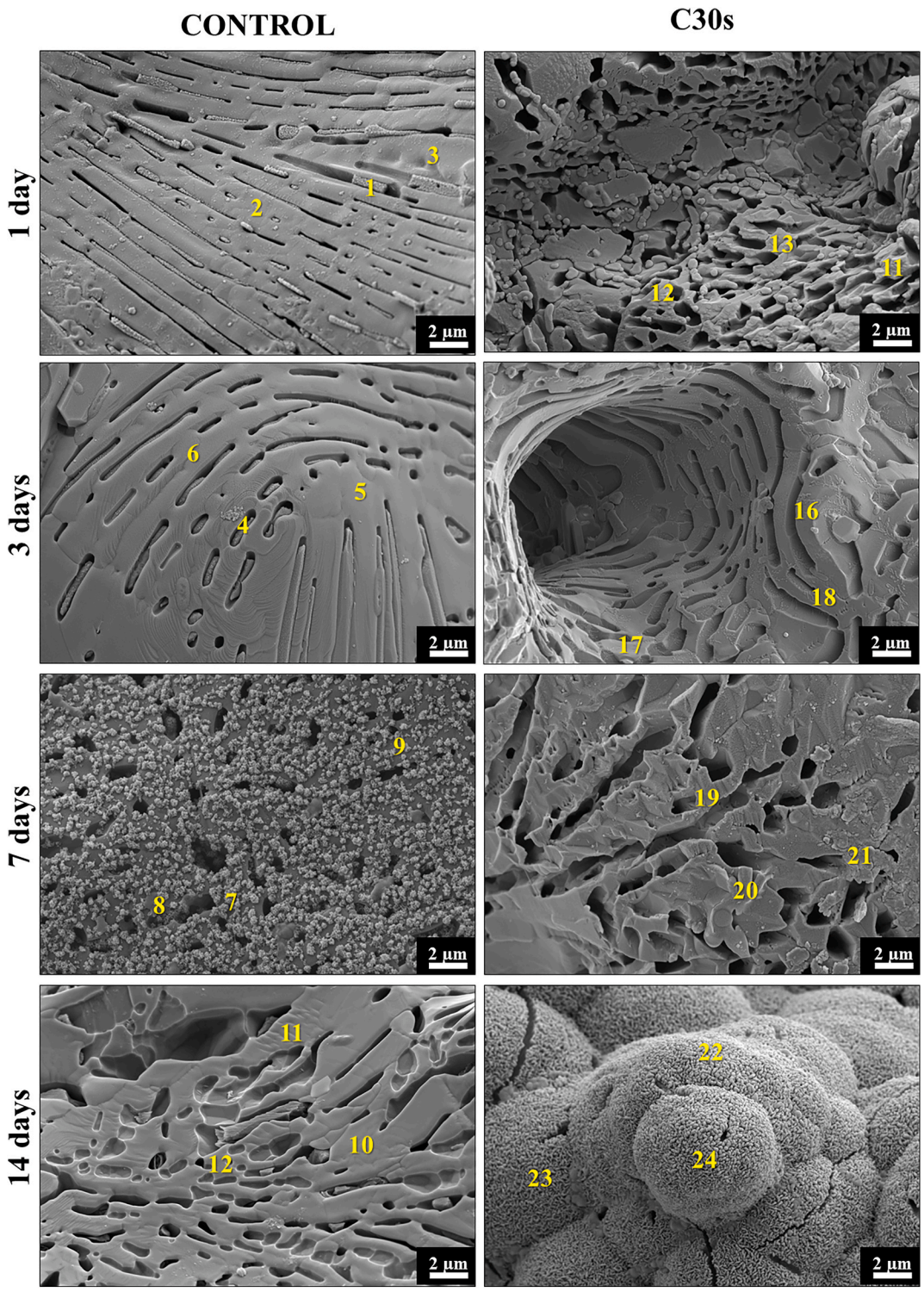

Fig. 4. FESEM images obtained after the in vitro bioactivity evaluation of control scaffolds and C30s scaffolds at 1, 3, 7 and 14 days.

of the scaffold surface and also colonized the interior part, demonstrating the growth of fibroblasts and extracellular matrix on the lamellar structure, along with a spherical precipitate very similar to HA.

4. Discussion

One of the essential aspects when developing materials for applications in personalized medicine is the interaction between cells and scaffold surface morphology, as this aspect allows modulation of cell adhesion, proliferation and differentiation. Consequently, lamellar microstructures are garnering significant attention [24]. Therefore, in this study, we have developed scaffolds based on a C_3S core and outer layers of $Ca_4Li_4(PO_4)_4$.

Once the scaffolds were sintered and analyzed by XRD, as shown in Fig. 1, the main phases observed were $Ca_2P_2O_7$, β-$Ca_3(PO_4)_2$, $Ca_{9.95}Li_{1.05}(PO_4)_7$, $CaLi(PO_4)$ and $Li_3(PO_4)$.

The β-$Ca_3(PO_4)_2$ phase is widely used in the development of materials for bone regeneration. It is one of the main and most common

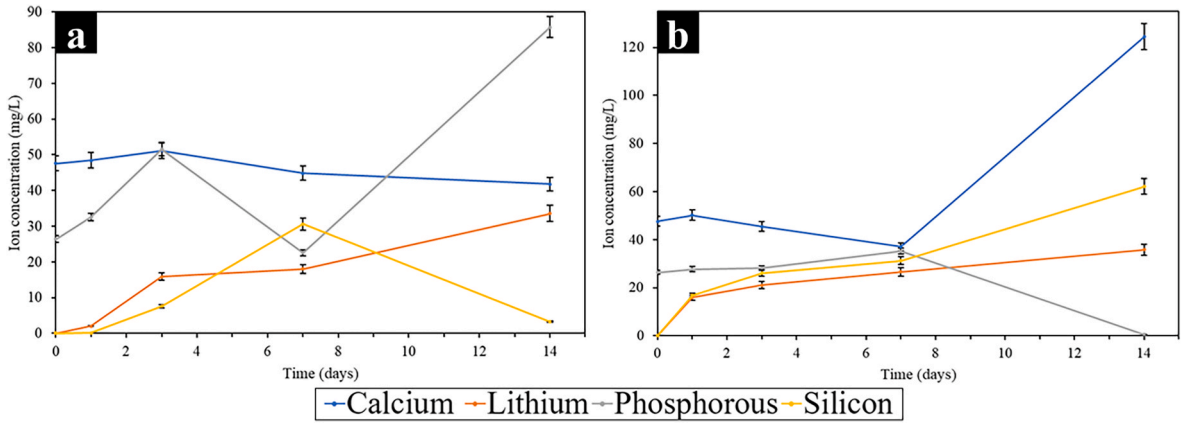

Fig. 5. The ion concentration in SBF at different times after soaking scaffolds: (a) Control and (b) C30s.

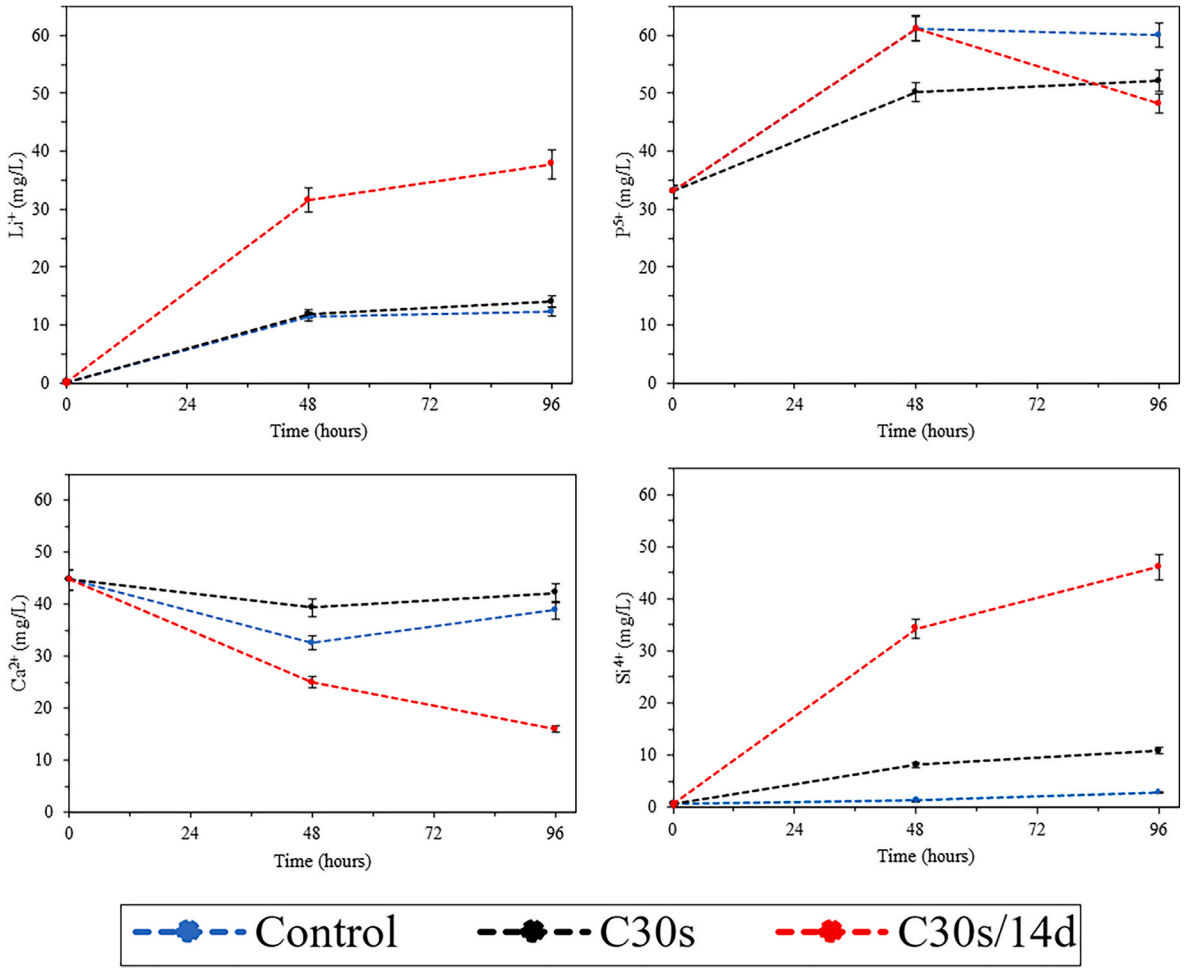

Fig. 6. Variation of the ionic concentration in the culture medium after coming into contact with the control, C30s and C30s/14d scaffolds at 50 mg/mL for 48 h and 96 h.

phases, which helps explain the behavior of the sintered scaffolds. The crystalline structure of β-TCP consists of a rhombohedral arrangement that, according to various studies, can be described in terms of columns A and B aligned along the C-axis. In this context, researchers have reported that column A is surrounded by six (6) column B, while column B is surrounded by two (2) column A and four (4) column B [25,26]. Column B comprises P(3), Ca(1), Ca(3), Ca(2) and P(2) sites, whereas column A consists of Ca(4), Ca(5) and P(1) sites, where the numbers in parentheses indicate different sites according to their degree of coordination with oxygen. Notably, column A exhibits a lower density due to the partial occupancy (43 %) of the Ca(4) sites, which facilitates the substitution of calcium ions by monovalent, divalent, or trivalent ions. [25,27]. In the synthesized scaffolds, Ca(4) sites were replaced by Li^{+} ions to maintain the electrical neutrality of the phase. Consequently, XRD analysis confirmed the presence of the main phase $Ca_{9.95}Li_{1.05}(PO_4)_7$, which is considered an isostructural variant of β-$Ca_3(PO_4)_2$

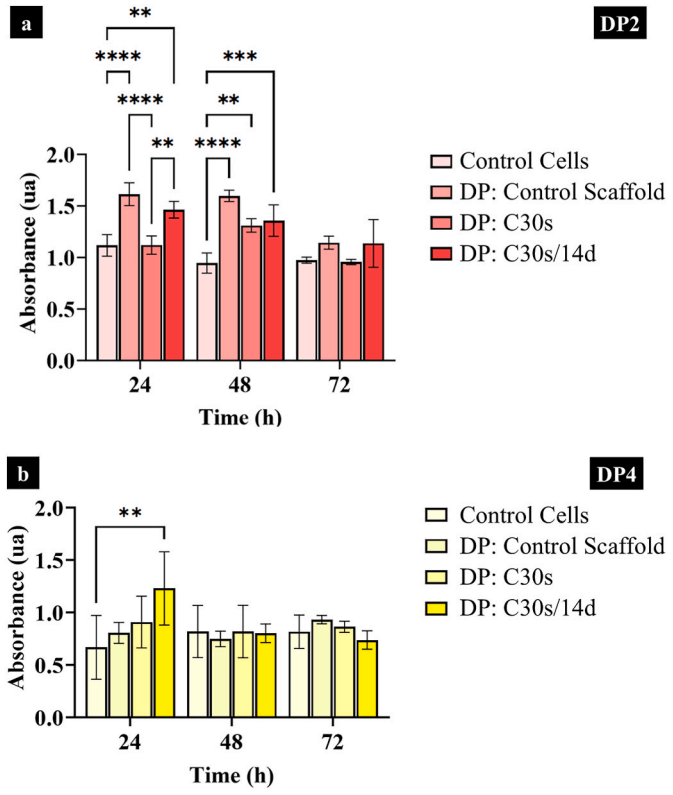

Fig. 7. Cell viability study of 3T3 cells after 24, 48 and 72 h incubated with DP2 and DP4, (a) and (b) respectively. Data were shown as means ± SD (n = 3, **p < 0.01, ***p < 0.001 and ****p < 0.0001).

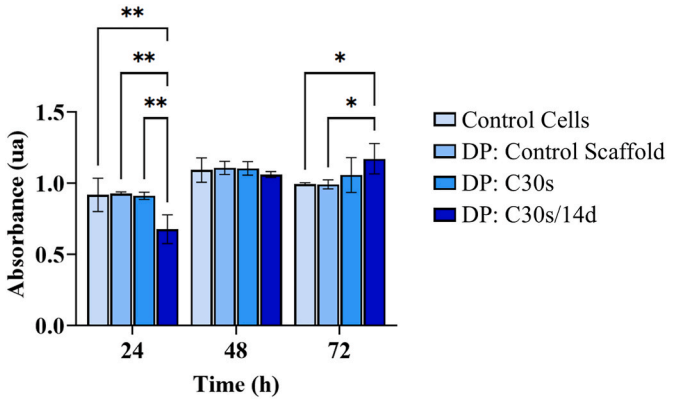

Fig. 8. Cell viability study of 3T3 cells after 24, 48 and 72 h incubated in contact with the Control, C30s and C30s/14d scaffolds. Data were shown as means ± SD (n = 3, *p < 0.05 and **p < 0.01).

[25,26]

Additionally, minor silicon phases, such as SiO_2, were detected, indicating that Ca^{2+} was released from the C_3S. This phenomenon suggests that the composition of the C_3S core serves as a Ca^{2+} source for the formation of calcium phosphate phases. As C_3S releases Ca^{2+} ions to the phosphate groups SiO_4^{4-} groups are obtained. To neutralize the negative charge associated with these groups, Si–O–Si bonds are formed, generating crystalline SiO_2. Additionally, Si–O–P and/or Si–O–Si bonds are produced, leading to the formation of an amorphous phase. This glass phase provides mechanical strength by binding the various crystalline phases together (Table 3).

This glass phase, as reported in the literature, is closely associated with lithium content, as lithium reduces viscosity, promotes phase separation, and influences overall microstructural organization. Consequently, lithium governs the formation, stability, and properties of the glassy matrix [28,29]. An increase in lithium content significantly enhanced the mechanical strength of the scaffold, with values 1.2 ± 0.1 MPa. Additionally, a high content of vitreous phase provided mechanical strength comparable to that of trabecular bone [30].

The microstructural arrangement of these phases, as shown in Fig. 2 (a–c), exhibits the presence of a lamellar microstructure. Although the presence of lamellae can be inferred, they appear to be covered by a film of the glass phase.

To eliminate the excess glass phase and reveal the lamellar microstructure, chemical etching was performed using a 3 % acetic acid solution, resulting in the C30s scaffolds. These scaffolds exhibited the same phases as the control scaffolds: $Ca_2P_2O_7$, β-$Ca_3(PO_4)_2$ and $Ca_{9.95}Li_{1.05}(PO_4)_7$. However, the XRD analysis of the C30s samples showed a significant decrease in the peaks corresponding to the $C_2P_2O_7$ phase. This behavior, previously reported in the literature, is related to the solubility of phases in an acid medium, where the Ca/P ratio plays a particularly important role. The general trend indicates that as the Ca/P ratio decreases, the dissolution rate increases. [31,32]. Accordingly, glass phases—$Ca_2P_2O_7$ and $CaLi(PO_4)$—exhibit a higher dissolution rate than β-$Ca_3(PO_4)_2$ and its isostructural compounds. Additionally, it is important to note that the substitution of Ca^{2+} by Li^+ enhances stability. Consequently, the $Ca_{9.95}Li_{1.05}(PO_4)_7$ phase is more stable than β-$Ca_3(PO_4)_2$ due to a reduction in the vacancies present in the latter.

Acid etching significantly influenced the physical properties of the scaffolds, primarily by increasing macroporosity and slightly reducing compressive strength due to a decrease in structural density resulting from the dissolution of the vitreous phase (Fig. 3) [33]. From a biological perspective, porosity plays a crucial role in cell proliferation and tissue formation. In terms of microporosity, no significant differences were observed between the materials, indicating that both are initially suitable for cell adhesion and growth factor retention. However, the increased macroporosity in the C30s scaffolds may enhance cell migration and vascularization, thereby promoting bone regeneration [34,35]. Furthermore, the C30s scaffolds exhibited a greater number of larger pores compared to the control, suggesting an overall increase in porosity, which could further support biological integration.

As for in vitro bioactivity (Fig. 4), the control scaffolds did not exhibit an HA-like precipitate owing to the inhibitory effect of the $Ca_2P_2O_7$ phase [36,37]. However, upon chemical etching and removal of the excess $Ca_2P_2O_7$ phase, an HA-like precipitate was observed on the C30s scaffolds at 14 days.

In addition, in the case of the bioactivity tests for the control sample, although no HA-like precipitates were observed, Fig. 4 shows that from day 1, surface changes indicative of degradation are present, appearing as an incipient lamellar microstructure. This is attributed to the hydrolysis process of phosphorus in the SBF and continues until day 3. This observation is corroborated by the phosphorus concentrations shown in Fig. 5 (a), which show an increase of phosphorus levels in the SBF from day 1 to day 3. Subsequently, this concentration decreases at 7 days, as the scaffold absorbs P ions and precipitates calcium phosphate in the form of small agglomerations on the degraded surface.

In contrast, the C30s samples showed a cauliflower-like HA-like precipitate at 14 days, with a Ca/P ratio of 1.68 ± 0.01, which is very similar to stoichiometric hydroxyapatite [36,38]. In this case, the ICP-OES results (Fig. 5 (b)) showed a decrease in P ion concentrations in the SBF, followed by an increase in Si ion concentrations. This mirrored behavior creates ideal conditions for HA-like precipitation on the scaffold. Moreover, at 14 days an increase in Ca ion concentration was observed, attributed to the release of Ca ions from silico-calcic minority phases during the release of Si ions.

As can be observed, different surface morphologies were obtained. Initially, a control scaffold with a smooth surface was produced. Later, after chemical etching for 30 s, a surface with a lamellar microstructure was obtained. Finally, when immersed in SBF, a rough surface rich in

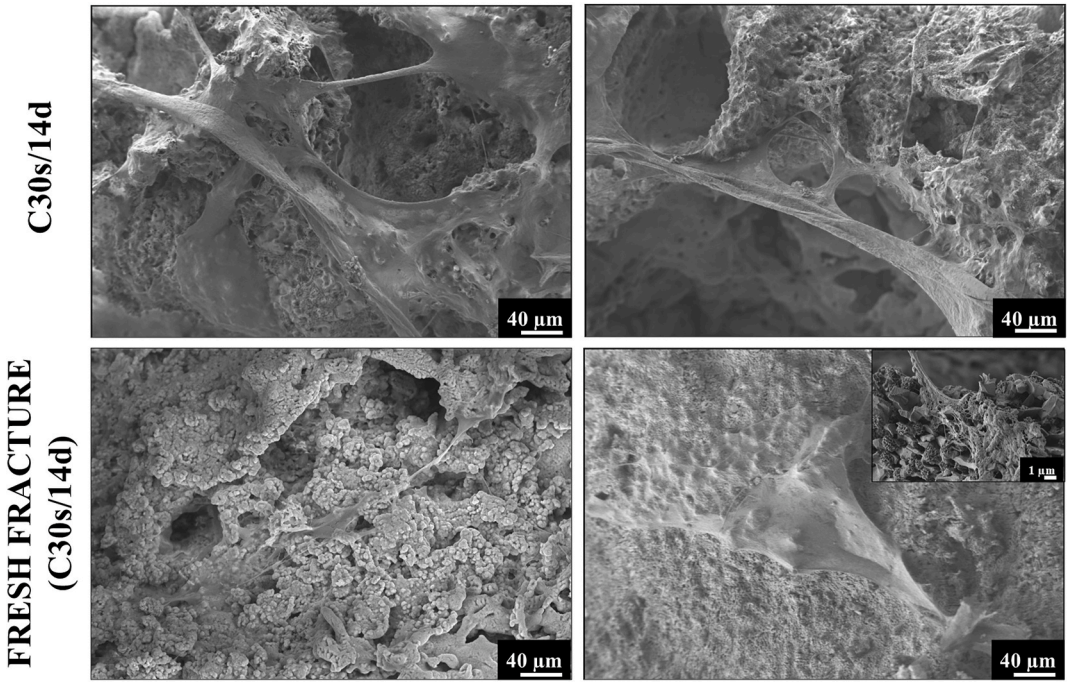

Fig. 9. FESEM images of the C30s/14d (surface and fresh fracture) after 72 h of immersion in the culture medium with 3T3 cells.

HA-like agglomerates was observed. Following this significant surface modulation, the scaffolds were tested biologically to evaluate cell behavior in response to surface modification and to assess the indirect effects of these scaffolds through the release of different ions.

Accordingly, the Alamar Blue assay was performed with 3T3 fibroblasts exposed to the scaffold (direct assay) and to its dissolution products (indirect assay), allowing the assessment of cytotoxicity and cell viability based on their metabolic activity in comparison with the control. Variations in the scaffold surface showed improved biological properties.

In the indirect assays (Fig. 7) performed on DP2 (a), significant differences were observed at 24 h between cells treated with traditional culture medium and the dissolution products obtained from the previously proposed scaffolds. However, it is important to highlight that for the DPs of the control scaffolds and the C30s/14d scaffolds the results obtained were significantly superior compared to the control cells. These DPs (Fig. 6) show similar behavior in Ca^{2+} and P^{5+} concentrations. At relatively short times—such as 24, 48, and 72 h—a slight increase in the concentration of P^{5+} can favor the proliferation and metabolic activity of fibroblasts, as it plays an important role in the synthesis of adenosine triphosphate (ATP) and energy supply [39,40]. Similarly, a slight increase in Li^{+} concentration is beneficial for cell cultures as it can stimulate cell proliferation through Wnt/β-catenin and enhance osteogenesis by improving cell differentiation [21,39,41,42] Finally, a slight increase in Si^{4+} concentrations in the culture medium may offer several advantages such as stimulation of collagen production for the formation of the extracellular matrix and stimulation of bone mineralization, leading to improvement in the biocompatibility of the scaffold [39,43,44].

In the case of DP4, the best results were obtained at 24 h for the C30s/14d scaffolds, indicated by higher absorbance and greater cell viability. At 48 and 72 h, the results exhibited a similar trend across all dissolution products (DPs). The findings from the dissolution products DP2 and DP4 are promising, as they are not toxic and promote cell proliferation.

Numerous researchers have studied the behavior of cells and their interaction with biomaterials, demonstrating the importance of the surface reactivity of bioactive ceramics and its influence on bone tissue formation [45,46]. In this regard, Fig. 8 at 72 h highlights the impact of the surface lamellar microstructure, as evidenced by the higher absorbance values observed in cells seeded on the C30s samples compared to those on the control scaffolds. This interaction affects the adhesion, proliferation, and differentiation of bone cells, playing a key role in osteointegration [45,47].

In the case of the direct assays (Fig. 8), reduced proliferation was observed in fibroblasts seeded on C30s/14d scaffolds at 24 h. However, this difference disappeared by 48 h, indicating the biocompatibility of the scaffolds. Nevertheless, when comparing the results obtained for the different scaffolds, higher cell growth was observed in the C30s/14d scaffolds, which even surpassed the control group at 72 h and the results of both the control and scaffold groups from earlier time points. These results suggest that the HA-like morphology precipitated in the lamellar microstructure induces higher cell proliferation.

Moreover, the presence of a lamellar microstructure is a key element in improving cell-material interaction. The lamellar architecture, revealed after acid etching, provides a topography that promotes cell adhesion. This structure, with nanometer-scale spacing (200–500 nm), may act as a physical guide for cell migration and ECM deposition, mimicking the stratified morphology of regenerating bone tissue. Therefore, the combination of this structure with the HA-like deposition on its surface is synergistic, promoting superior bioactivity in C30s/14d scaffolds. Furthermore, the colonization observed in the inner areas of the scaffold suggests that the lamellar structure facilitates on surface adhesion and deep cell infiltration, a crucial aspect for effective three-dimensional tissue regeneration.

Finally, the C30s/14d scaffolds at 72 h were treated and observed by FESEM, as shown in Fig. 9. The image reveals how cells have colonized the scaffold surface—both the HA-like and lamellar microstructures—as well as the internal scaffold structure due to the its porosity. Cellular colonization and partial ECM formation on the lamellar microstructure and the HA-like precipitate are clearly observed.

5. Conclusions

The behavior of cells within the lamellar microstructure of multilayer porous 3D scaffolds—primarily composed of the phases $Ca_{9.95}Li_{1.05}(PO_4)_7$ and β-$Ca_3(PO_4)_2$—developed through the sol-gel process,

was investigated.

This cellular behavior was investigated using 3T3 fibroblast cells. To evaluate how the cells respond to surface morphology modulation in 3D multilayer porous scaffolds, three types of surfaces were obtained: control scaffolds, chemically etched scaffolds (C30s), and chemically etched scaffolds with HA-like deposit (C30s/14d), the latter more closely mimicking the surface morphology of bone.

Notably, none of the samples studied exhibited cytotoxicity. The exposure of a lamellar microstructure through chemical etching proved to be a key factor in enhancing the biological performance of the scaffolds. This architecture contributed not only to increased macroporosity and ion exchange but also provided a biomimetic surface topography that promoted improved cell adhesion, proliferation, and infiltration. Furthermore, direct cell viability studies showed an increase in cell proliferation from 24 to 72 h in the C30s scaffolds. This effect was more pronounced when the cells were in contact with the C30s/14d scaffolds, suggesting that the HA-like deposit within the lamellar microstructure enhances cell development.

In addition, indirect studies were conducted using the dissolution products of the scaffolds at 48 h (DP2) and 96 h (DP4), where the release of Li, P, and Si ions was observed. A general trend of cell proliferation was noted when the cells were in contact with the dissolution products. However, it is important to highlight that the 3T3 cell line exhibited greater growth at 48 h with the dissolution products (DP2) across all scaffolds, while for DP4, better cellular behavior was observed at shorter exposure times.

In summary, the lamellar microstructure, achieved through surface modulation, plays a critical and functional role in the biointegration of these scaffolds, positioning them as promising candidates for applications in bone tissue engineering.

CRediT authorship contribution statement

M. Angélica Barbudo: Writing – original draft, Investigation, Formal analysis, Conceptualization. **Pablo Velásquez:** Software, Methodology, Formal analysis. **Ángel Murciano:** Writing – review & editing, Writing – original draft, Methodology, Investigation, Formal analysis, Conceptualization. **Piedad N. De Aza:** Writing – review & editing, Validation, Supervision, Resources, Project administration, Funding acquisition, Formal analysis.

Funding

This work is part of the project PID2020-116693RB-C21, funded by MCIN/AEI/10.13039/501100011033 Spain.

Declaration of competing interest

The authors declare that they have no known competing financial interests or personal relationships that could have appeared to influence the work reported in this paper.

Acknowledgments

The Ph.D. student M. Angélica Barbudo has been funded by a grant from the Government of Generalitat Valenciana with reference CIGRIS/2022/190. We are sincerely grateful to M. Desiree González Gras for her valuable technical support during the cellular studies.

Appendix A. Supplementary data

Supplementary data to this article can be found online at https://doi.org/10.1016/j.ceramint.2025.06.145.

References

[1] P. Sharma, P. Kumar, R. Sharma, V.D. Bhatt, P.S. Dhot, Tissue engineering; current status & futuristic scope, J. Med. Life. 12 (2019) 225–229, https://doi.org/10.25122/jml-2019-0032.

[2] L. Roseti, V. Parisi, M. Petretta, C. Cavallo, G. Desando, I. Bartolotti, B. Grigolo, Scaffolds for bone tissue engineering: state of the art and new perspectives, Mater. Sci. Eng. C 78 (2017) 1246–1262, https://doi.org/10.1016/j.msec.2017.05.017.

[3] C. Zhao, W. Liu, M. Zhu, C. Wu, Y. Zhu, Bioceramic-based scaffolds with antibacterial function for bone tissue engineering: a review, Bioact. Mater. 18 (2022) 383–398, https://doi.org/10.1016/j.bioactmat.2022.02.010.

[4] M.P. Nikolova, M.S. Chavali, Recent advances in biomaterials for 3D scaffolds: a review, Bioact. Mater. 4 (2019) 271–292, https://doi.org/10.1016/j.bioactmat.2019.10.005.

[5] R. Kumar, I. Pattanayak, P.A. Dash, S. Mohanty, Bioceramics: a review on design concepts toward tailor-made (multi)-functional materials for tissue engineering applications, J. Mater. Sci. 58 (2023) 3460–3484, https://doi.org/10.1007/s10853-023-08226-8.

[6] F. Barrère, M. Ni, P. Habibovic, P. Ducheyne, K. de Groot, Degradation of bioceramics, in: C.A. Van Blitterswijk, P. Thomsen, A. Lindahl, J. Hubbell, D. F. Williams, R. Cancedda, et al. (Eds.), Tissue Engineering, Academic Press: Elsevier Inc., Amsterdam, 2008, pp. 223–254, https://doi.org/10.1016/b978-0-12-370869-4.00008-2.

[7] Z. Sheikh, S. Najeeb, Z. Khurshid, V. Verma, H. Rashid, M. Glogauer, Biodegradable materials for bone repair and tissue engineering applications, Materials 8 (2015) 5744–5794, https://doi.org/10.3390/ma8095273.

[8] G. Kirmizidis, M. Res, M.A. Birch, Microfabricated grooved substrates influence cell-cell communication and osteoblast differentiation in vitro, Tissue Eng. Part. A. 15 (2009) 1427–1436, https://doi.org/10.1089/ten.tea.2008.0137.

[9] P. Ros-Tárraga, P. Mazón, M.A. Sainz, L. Meseguer-Olmo, P.N. De Aza, Surface modifications of a diopside–wollastonite eutectic ceramic after acellular and cellular in vitro tests, Surf. Coating. Technol. 378 (2019) 124965, https://doi.org/10.1016/j.surfcoat.2019.124965.

[10] R.-R. Ruben, R.-N. Beatriz, M. Patricia, A.-C. Salvador, R.-T. Patricia, N.D. Piedad, M.-O. Luis, Impact of a porous Si-Ca-P monophasic ceramic on variation of osteogenesis-related gene expression of adult human mesenchymal stem cells, Applied Sciences 8 (2018), https://doi.org/10.3390/app8010046.

[11] P. Ros-Tárraga, P. Mazón, B. Revilla-Nuin, R. Rabadán-Ros, P.N. de Aza, L. Meseguer-Olmo, High temperature $CaSiO_3$–$Ca_3(PO_4)_2$ ceramic promotes osteogenic differentiation in adult human mesenchymal stem cells, Mater. Sci. Eng. C 107 (2020) 110355, https://doi.org/10.1016/j.msec.2019.110355.

[12] D. Xiao, J. Zhang, C. Zhang, D. Barbieri, H. Yuan, L. Moroni, G. Feng, The role of calcium phosphate surface structure in osteogenesis and the mechanisms involved, Acta Biomater. 106 (2020) 22–33, https://doi.org/10.1016/j.actbio.2019.12.034.

[13] S. Lenhert, M.B. Meier, U. Meyer, L. Chi, H.P. Wiesmann, Osteoblast alignment, elongation and migration on grooved polystyrene surfaces patterned by langmuir-blodgett lithography, Biomaterials 26 (2005) 563–570, https://doi.org/10.1016/j.biomaterials.2004.02.068.

[14] Y. Zhu, K. Zhang, R. Zhao, X. Ye, X. Chen, Z. Xiao, et al., Bone regeneration with micro/nano hybrid-structured biphasic calcium phosphate bioceramics at segmental bone defect and the induced immunoregulation of MSCs, Biomaterials 147 (2017) 133–144, https://doi.org/10.1016/j.biomaterials.2017.09.018.

[15] S. Bauer, P. Schmuki, K. von der Mark, J. Park, Engineering biocompatible implant surfaces: part I: materials and surfaces, Prog. Mater. Sci. 58 (2013) 261–326, https://doi.org/10.1016/j.pmatsci.2012.09.001.

[16] I. Ielo, G. Calabrese, G. De Luca, S. Conoci, Recent advances in hydroxyapatite-based biocomposites for bone tissue regeneration in orthopedics, Int. J. Mol. Sci. 23 (2022), https://doi.org/10.3390/ijms23179721.

[17] E. Martínez, E. Engel, J.A. Planell, J. Samitier, Effects of artificial micro- and nano-structured surfaces on cell behaviour, Ann. Anat. 191 (2009) 126–135, https://doi.org/10.1016/j.aanat.2008.05.006.

[18] M.V. Plikus, X. Wang, S. Sinha, E. Forte, S.M. Thompson, E.L. Herzog, et al., Fibroblasts: origins, definitions, and functions in health and disease, Cell 184 (2021) 3852–3872, https://doi.org/10.1016/j.cell.2021.06.024.

[19] S. Vahabzadeh, V.K. Hack, S. Bose, Lithium-doped β-tricalcium phosphate: effects on physical, mechanical and in vitro osteoblast cell–material interactions, J. Biomed. Mater. Res. B Appl. Biomater. 105 (2017) 391–399, https://doi.org/10.1002/jbm.b.33485.

[20] V.V. Smirnov, S.V. Smirnov, A.I. Krylov, O.S. Antonova, M.A. Goldberg, T. O. Obolkina, et al., Influence of lithium on the structure and phase composition formation in the synthesis of hydroxyapatite, Dokl. Chem. 481 (2018) 177–180, https://doi.org/10.1134/S0012500818080025.

[21] P. Han, C. Wu, J. Chang, Y. Xiao, The cementogenic differentiation of periodontal ligament cells via the activation of Wnt/β-catenin signalling pathway by li^+ ions released from bioactive scaffolds, Biomaterials 33 (2012) 6370–6379, https://doi.org/10.1016/j.biomaterials.2012.05.061.

[22] P. Ros-Tárraga, A. Murciano, P. Mazón, S.A. Gehrke, P.N. De Aza, New 3D stratified Si-Ca-P porous scaffolds obtained by sol-gel and polymer replica method: microstructural, mineralogical and chemical characterization, Ceram. Int. 43 (2017) 6548–6553, https://doi.org/10.1016/j.ceramint.2017.02.081.

[23] T. Kokubo, H. Takadama, How useful is SBF in predicting in vivo bone bioactivity? Biomaterials 27 (2006) 2907–2915, https://doi.org/10.1016/j.biomaterials.2006.01.017.

[24] A. Díaz-Arca, P. Mazón, P.N. De Aza, Eutectoid scaffold as a potential tissue engineer guide, J. Am. Ceram. Soc. 102 (2019) 7168–7177, https://doi.org/10.1111/jace.16639.

[25] K. Yoshida, H. Hyuga, N. Kondo, H. Kita, M. Sasaki, M. Mitamura, et al., Substitution model of monovalent (li, Na, and K), divalent (mg), and trivalent (al) metal ions for β-tricalcium phosphate, J. Am. Ceram. Soc. 89 (2006) 688–690, https://doi.org/10.1111/j.1551-2916.2005.00727.x.

[26] V.A. Morozov, A.A. Belik, R.N. Kotov, et al., Crystal structures of double calcium and alkali metal phosphates Ca_{10} $M(PO_4)_7$(M = Li, Na, K), Crystallogr. Rep. 45 (2000) 13–20, https://doi.org/10.1134/1.171129.

[27] N. Matsumoto, K. Yoshida, K. Hashimoto, Y. Toda, Thermal stability of β-tricalcium phosphate doped with monovalent metal ions, Mater. Res. Bull. 44 (2009) 1889–1894, https://doi.org/10.1016/j.materresbull.2009.05.012.

[28] H. Al-Johani, J. Haider, J. Satterthwaite, N. Silikas, Lithium silicate-based glass ceramics in dentistry: a narrative review, Prosthesis 6 (2024) 478–505, https://doi.org/10.3390/prosthesis6030034.

[29] N. Monmaturapoj, P. Lawita, W. Thepsuwan, Characterisation and properties of lithium disilicate glass ceramics in the SiO_2-Li_2O-K_2O-Al_2O_3 system for dental applications, Adv. Mater. Sci. Eng. (2013) 1–11, https://doi.org/10.1155/2013/763838.

[30] L.J. Gibson, M.F. Ashby, Cellular Solids: Structure and Properties, second ed., Pergamon, Oxford, 1999, pp. 429–452.

[31] L. Wang, G.H. Nancollas, Calcium orthophosphates: crystallization and dissolution, Chem. Rev. 108 (2008) 4628–4669, https://doi.org/10.1021/cr0782574.

[32] N. Matsumoto, K. Yoshida, K. Hashimoto, Y. Toda, Dissolution mechanisms of β-tricalcium phosphate doped with monovalent metal ions, J. Ceram. Soc. Jpn. 118 (2010) 451–457.

[33] S. Lee, S. Yang, I. Bajpai, I.K. Kang, S. Kim, Enhancement of the pore interconnectivity and porosity of calcium phosphate scaffolds by acid-etching method, Acta Metall. Sin. 28 (2015) 1109–1116, https://doi.org/10.1007/s40195-015-0301-1.

[34] S. Bose, S. Tarafder, Calcium phosphate ceramic systems in growth factor and drug delivery for bone tissue engineering: a review, Acta Biomater. 8 (2012) 1401–1421, https://doi.org/10.1016/j.actbio.2011.11.017.

[35] B. Bisht, A. Hope, A. Mukherjee, M.K. Paul, Advances in the fabrication of scaffold and 3D printing of biomimetic bone graft, Ann. Biomed. Eng. 49 (2021) 1128–1150, https://doi.org/10.1007/s10439-021-02752-9.

[36] M. Canillas, P. Pena, A.H. De Aza, M.A. Rodríguez, Calcium phosphates for biomedical applications, Bol. Soc. Espanola Ceram. Vidr. 56 (2017) 91–112, https://doi.org/10.1016/j.bsecv.2017.05.001.

[37] I.R. Orriss, T.R. Arnett, R.G.G. Russell, Pyrophosphate: a key inhibitor of mineralisation, Curr. Opin. Pharmacol. 28 (2016) 57–68, https://doi.org/10.1016/j.coph.2016.03.003.

[38] Shi Donglu, Introduction to Biomaterials, Tsinghua University Press, 2006.

[39] Y. Su, M. Cappock, S. Dobres, A.J. Kucine, W.C. Waltzer, D. Zhu, Supplemental mineral ions for bone regeneration and osteoporosis treatment, Eng. Regen. 4 (2023) 170–182, https://doi.org/10.1016/j.engreg.2023.02.003.

[40] J.W.F. Nicholls, J.P. Chin, T.A. Williams, T.M. Lenton, V. O'Flaherty, J. W. McGrath, On the potential roles of phosphorus in the early evolution of energy metabolism, Front. Microbiol. 14 (2023), https://doi.org/10.3389/fmicb.2023.1239189.

[41] L. Li, X. Peng, Y. Qin, R. Wang, J. Tang, X. Cui, et al., Acceleration of bone regeneration by activating Wnt/β-catenin signalling pathway via lithium released from lithium chloride/calcium phosphate cement in osteoporosis, Sci. Rep. 7 (2017), https://doi.org/10.1038/srep45204.

[42] N. Kurgan, K.N. Bott, W.E. Helmeczi, B.D. Roy, I.D. Brindle, P. Klentrou, et al., Low dose lithium supplementation activates Wnt/β-catenin signalling and increases bone OPG/RANKL ratio in mice, Biochem. Biophys. Res. Commun. 511 (2019) 394–397, https://doi.org/10.1016/j.bbrc.2019.02.066.

[43] R. Jugdaohsingh, Silicon and bone health, J. Nutr. Health Aging 11 (2007) 99–110.

[44] W. Götz, E. Tobiasch, S. Witzleben, M. Schulze, Effects of silicon compounds on biomineralization, osteogenesis, and hard tissue formation, Pharmaceutics 11 (2019), https://doi.org/10.3390/pharmaceutics11030117.

[45] P. Ducheyne, Q. Qiu, Bioactive ceramics: the effect of surface reactivity on bone formation and bone cell function, Biomaterials 20 (1999) 2287–2303, https://doi.org/10.1016/S0142-9612(99)00181-7.

[46] H. Amani, H. Arzaghi, M. Bayandori, A.S. Dezfuli, H. Pazoki-Toroudi, A. Shafiee, et al., Controlling cell behavior through the design of biomaterial surfaces: a focus on surface modification techniques, Adv. Mater. Interfaces. 6 (2019), https://doi.org/10.1002/admi.201900572.

[47] A.B.G. De Carvalho, M. Rahimnejad, R.L.M.S. Oliveira, P. Sikder, G.S.F. A. Saavedra, S.B. Bhaduri, et al., Personalized bioceramic grafts for craniomaxillofacial bone regeneration, Int. J. Oral Sci. 16 (2024), https://doi.org/10.1038/s41368-024-00327-7.